

Neutron Radiographic Study of the Effect of Heat-Driven Water Transport on the Tensile Strength of Bentonite-Bonded Moulding Sand

Korbinian Schiebel¹ · Guntram Jordan¹ · Anders Kaestner² · Burkhard Schillinger³ · Sandra Boehnke⁴ · Wolfgang W. Schmahl¹

Received: 21 March 2017 / Accepted: 10 November 2017 / Published online: 21 November 2017
© The Author(s) 2017. This article is an open access publication

Abstract Wet tensile testing is a common method to assess the stability of bentonite-bonded moulding sands. For wet tensile testing, a specimen is first heated from above in order to simulate heat-driven moisture transport induced by the casting process. Then, tensile stress is applied until rupture. In this study, neutron radiography imaging was applied to moulding sands in situ during heating and wet tensile testing in order to investigate the effects of water kinematics on the tensile strength. Neutron radiography allowed the localization of the rupture plane and the quantitative determination of the local water content with sub-mm resolution. Quantification of the temperature at the rupture plane and of the heat kinematics within the specimen was accomplished by temperature measurements both in situ and ex situ. In this way, experimental data correlating the wet tensile strength with the specific conditions of moulding sands at the rupture plane were obtained for the first time. Series of experiments with different initial sand moisture contents were conducted. The results show

✉ Guntram Jordan
jordan@lmu.de

Korbinian Schiebel
Korbinian.Schiebel@lrz.uni-muenchen.de

Anders Kaestner
anders.kaestner@psi.ch

Burkhard Schillinger
burkhard.schillinger@frm2.tum.de

Sandra Boehnke
sandra.boehnke@imerys.com

Wolfgang W. Schmahl
Wolfgang.W.Schmahl@lrz.uni-muenchen.de

¹ Department für Geo- und Umweltwissenschaften, Ludwig-Maximilians-Universität München, Theresienstrasse 41, 80333 Munich, Germany

² Paul Scherrer Institute (PSI), WBBA/110, 5232 Villigen, Switzerland

³ Forschungs-Neutronenquelle Heinz Maier-Leibnitz, Lichtenbergstr. 1, 85748 Garching, Germany

⁴ Imerys Metalcasting Germany GmbH, Schmielenfeldstr. 78, 45772 Marl, Germany

that the weakest location within a sand profile can be pinpointed at the interface between evaporation and condensation zone (i.e. at the 100 °C isotherm), where water vaporization starts and the water bridges connecting the sand grains collapse. This weakest location has maximum strength, if the local water content at the rupture plane is between 5 and 9 wt.%. Less water leads to a strong decrease of wet tensile strength. More water requires an initial water content above 5 wt.%, which leads to a decrease of the tensile strength of the unheated sand.

Keywords Bentonite · Smectite · Moulding sand · Dehydration · Porous media · Neutron radiography · Casting defects · Foundry industry

1 Introduction

Commonly, bentonite is used as a component of building materials in geoengineering (Harvey and Murray 1997; Wolters et al. 2015) and as binder for ceramics and moulding sands (Odom 1984). In foundry industries, bentonite-bonded quartz sand is one of the most frequently used mould materials. The mechanical properties of bentonite-bonded sand moulds strongly depend on temperature, the amount of water, and the mineralogical composition of the bentonite (Grim and Guven 1978). During casting, a temperature gradient is induced within the sand mould. Water near the mould cavity evaporates and migrates into the colder mould interior where it condenses. As the heat advances deeper into the mould, water continues to evaporate and migrates even further. The resulting total heat and moisture transport, therefore, is composed of a number of different individual processes like heat conduction and convection, water vaporization and condensation (Kubo and Pehlke 1986) as well as water uptake and release within the interlayer space of the clay minerals (smectites) composing the bentonite.

The spatial and temporal gradients of heat and water concentration within the mould result in mobile zones of different mechanical properties, notably of different tensile strength (Patterson and Boenisch 1964), of the mould material. In the condensation zone facing away from the melt, increasing moisture causes a significant decrease of tensile strength. In the hot sand layers facing towards the melt, i.e. the dry zone, quartz crystals expand and compressive stress arises. Together, the decrease of tensile strength and the increase of compressive stress are assumed to cause spalling of sand layers—especially at the top of the mould cavity. The casting flaws of the metal parts resulting from these defective moulds are called scabs, which are among the most frequently occurring casting defects associated with bentonite-bonded sands (Campbell 2011). However, in contrast to other types of moulding sands with lower scabbing tendencies, bentonite-bonded sand has an excellent environmental performance and is largely reusable. Motivation for the present study, therefore, is to contribute to the improvement of the most sustainable mould material by acquiring fundamental scientific knowledge of the effects of heat-driven moisture transport on the mechanical properties of bentonite-bonded moulding sand.

The quality of bentonite-bonded sand in general and the tendency towards scabbing in particular can be determined by the ratio of compressive strength and wet tensile strength (Patterson and Boenisch 1964). In the industrial practice, the most common method of assessment of the mould performance during casting is wet tensile testing (BDG 1997). For this, a specimen (standardized in dimension and compaction) is heated from above (heater temperature = 310 °C). The heat induces temperature and moisture gradients within the sample. Once

the condensation zone approximately reaches an intended position within the sand specimen, tensile strength is measured. In spite of the common use of wet tensile testing in industries (Campbell 2011), water and heat kinematics within the specimen were never quantitatively measured in situ during wet tensile testing. Thus, the dependencies of fracture plane position and tensile strength on moisture and temperature were never determined precisely. Aim of this study, therefore, was to follow the location of the weakest point within the moulding sand quantitatively during time and to determine the effects of heat and water kinematics on fracture location and tensile strength.

In the past, high-precision in situ measurements of heat-driven moisture transfer within porous media were extremely challenging. Due to recent advances, neutron radiography became a powerful method to determine the water kinematics within porous media quantitatively (Schillinger et al. 2006; Kaestner et al. 2008). The attenuation of neutrons by most elements forming silicate minerals (Si, Al, Ca, Fe, Mg, Na, O ...) is orders of magnitudes smaller than attenuation by hydrogen. Neutron radiography, therefore, can quantify water transfer within porous media such as quartz sands, concretes, plants, rocks and soils in situ (Hassanein et al. 2006; Shokri et al. 2008; Schillinger et al. 2011; Sedighi-Gilani et al. 2013; Shokri and Or 2013; Hall 2013; Jordan et al. 2013; Villman et al. 2014; Boon et al. 2015). In combination with temperature measurements and mechanical testing, neutron radiography is not only a suitable method to investigate the coupling of heat and moisture transport but also to assess the relation between transport and material property. Furthermore, if water is the only mobile phase, plots of local moisture content vs. temperature can be taken as local thermogravimetric measurements within a large-scale sample (Jordan et al. 2013).

2 Experimental

For the in situ measurements of the water kinematics during wet tensile testing, a tensile testing apparatus was constructed which is compatible with simultaneous exposure to neutron radiation. Neutron radiography time series were performed both at the cold neutron imaging facility ICON [SINQ, Paul Scherrer Institute, Villigen, Switzerland, (Kaestner et al. 2011)] and at the imaging beamline ANTARES [FRM II, Heinz Maier-Leibnitz Zentrum, Garching, Germany, (Schulz and Schillinger 2015)]. At ICON tensile testing was followed using a sCMOS camera (image frequency: 4 frames per second, field of view: 105 mm × 72 mm, spatial resolution 0.047 mm/pixel, ample detector distance 4 cm). At ANTARES, tensile testing was imaged with a CMOS camera (image frequency: 0.55 frames per second, field of view: 100 mm × 80 mm, spatial resolution 0.047 mm/pixel, sample detector distance 12 cm).

Green sand consisting of quartz (average grain size approx. 0.3 mm) and 8 wt.% of natural sodium bentonite (Wyoming) was obtained from S&B Minerals (Imerys, Marl, Germany). The sand has been dried at 120 °C for at least 24 h before it was remoistened with defined water quantities (2, 3, 4, and 5 wt.% H₂O) and aged for at least 24 h in air-tight bags. The aged sand, then, was sieved into a two-part aluminium specimen tube (Fig. 1). The lower prismatic part of the specimen tube has a quadratic 44 mm × 44 mm cross section and a height of 100 mm. The quadratic cross section of the upper pyramidal part (height 20 mm) increased from 44 mm × 44 mm to 54 mm × 54 mm. The aluminium walls of the tube (thickness 3 mm) were almost transparent in the neutron radiographs. The two-part specimen tube was turned upside down and filled with sieved sand. Subsequently, the sand within the tube was compressed with 1 MPa. Compaction depth Δy_C was measured to determine the sample volume and to calculate porosity Φ and saturation S . For this, porosity and saturation are defined by:

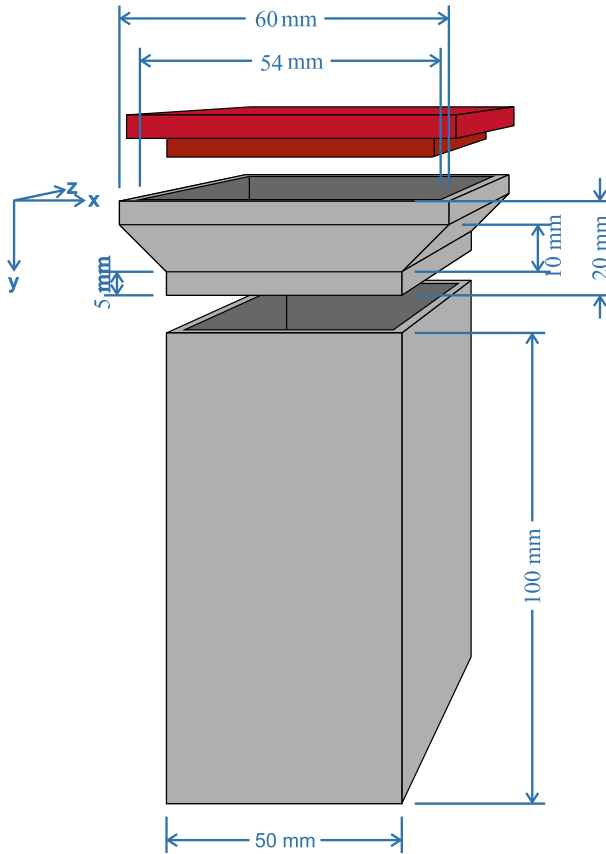


Fig. 1 Sketch of the two-part specimen tube and the heating plate used for the wet tensile testing

$$\Phi = \frac{V_{St} - \Delta y_C A - m_S / \rho_S}{V_{St} - \Delta y_C A} \tag{1}$$

(V_{St} is the volume of the complete sample tube, m_S is the mass of the dry sand, ρ_S is the density of the dry sand, A is the cross-sectional area of the lower sample tube), and

$$S = \frac{m_W / \rho_W}{V_{St} - \Delta y_C A - m_S / \rho_S} \tag{2}$$

(ρ_W is the density of water; m_W is the mass of water), respectively.

To induce moisture and temperature gradients within the sample, the sand was contacted from above with a heater which had been preheated to 310 °C according to VDG norm P38 (BDG 1997). After a defined heating period, tensile force was increased by 50 N/s and continuously measured by a stress gauge with a frequency of 200 data points per second. After rupture, the tensile strength σ_t was determined by subtracting the weight of the upper sample part F_g (specimen and specimen tube) from the maximum measured tensile force F_r and normalizing this net tensile force to the cross-sectional area A at the specimen neck.

$$\sigma_t = \frac{F_r - F_g}{A} \tag{3}$$

Thermocouples provided temperature data integrated over a sample volume of several cubic millimetres. Temperature gradients on the scale of individual sand grains and pores (filled or unfilled) were not accessible. The comparison of temperature measurements at a given position in different experiments performed under same conditions (moisture, porosity) showed that a temperature can be assigned to a certain position with an accuracy of approximately ± 2.5 mm. This limited spatial resolution mainly results from the low accuracy of the determination of the thermocouple position in the radiographs.

The evolution of the local temperature was continuously measured during the experiments at four different positions below the specimen neck with a frequency of two measurements per second. In order to determine the temperature distribution in the upper pyramidal part, additional reference experiments without tensile testing were conducted. The local temperature, thereby, was measured in steps of 5 mm from the heating plate with a frequency of two measurements per second for at least 330 s.

3 Image Analysis

The local transmission $\tau(x, y)$ of a parallel neutron beam through a specimen in beam direction z is given by Beer–Lambert law:

$$\tau(x, y, t) = \frac{I(x, y, t)}{I_0(x, y)} = e^{-\sum_i \Delta z_i(x, y, t)} \tag{4}$$

where $I(x, y, t)$ and $I_0(x, y)$ are the transmitted and the initial intensity, respectively, at the pixel position x, y and time t . Σ_i is the macroscopic cross section of phase i , and $\Delta z_i(x, y, t)$ is the thickness of phase i in beam direction z . The initial intensity at each pixel $I_0(x, y)$ is determined by the median intensity of 10 open beam images. To eliminate the influence camera offset and dark current, all images were black field corrected. Therefore, at each pixel (x, y) the median intensity of 10 dark images $I_d(x, y)$ was subtracted from each experimental radiograph as well as from the open beam images:

$$\tau(x, y, t)^{\text{Cor}} = \frac{I(x, y, t) - I_d(x, y)}{I_0(x, y) - I_d(x, y)} \tag{5}$$

Intensity fluctuations of the neutron beam while taking the radiography image sequence were corrected by an individual image correction factor $b(t)$ according to Hassanein (2006). The factor equals the ratio of the average brightness of an open beam area $I(x_o, y_o, t)$ within a radiograph and the average brightness of the same area in the open beam images $I_0(x_o, y_o)$. Additionally, the factor has to include a black field correction for the selected area $I_d(x_o, y_o)$ which needs to be subtracted from both values:

$$b(t) = \frac{I(x_o, y_o, t) - I_d(x_o, y_o)}{I_0(x_o, y_o) - I_d(x_o, y_o)} \tag{6}$$

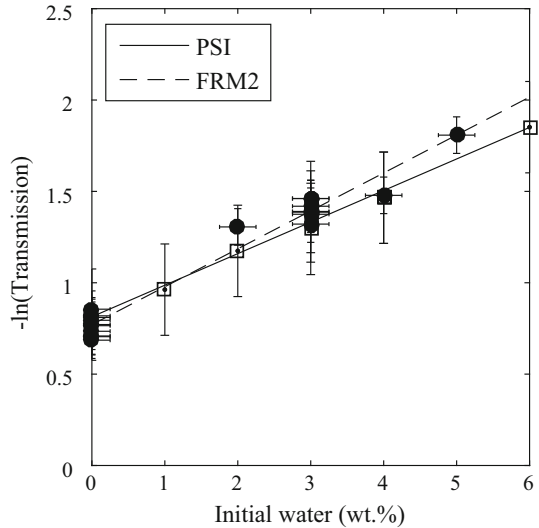
The transmission then is:

$$\tau^{\text{Cor}}(x, y, t) = \frac{I(x, y, t) - I_d(x, y)}{I_0(x, y) - I_d(x, y)} / b(t) \tag{7}$$

Using the above corrections, the measured neutron transmission can be correlated with the water thickness $\Delta z_W(x, y, t)$ in a porous medium like quartz sand:

$$\ln(\tau^{\text{Cor}}(x, y, t)) = -\Delta z_S \Sigma_S - \Delta z_W(x, y, t) \Sigma_W \tag{8}$$

Fig. 2 Negative natural logarithm of the corrected and normalized neutron transmissions $-\ln(\tau^{\text{Cor,Nor}})$ against sand moisture for a sample thickness of 50 mm (44-mm sand, 2×3 -mm aluminium). Linear regressions of the transmissions measured at the two neutron beam lines are inserted (PSI solid line, empty symbols; FRM II dashed line, filled symbols). The correlation factor Θ_W can be determined by the slope of the linear regressions. The negative natural logarithm of the transmission through the dry sand $-\ln(\tau_S^{\text{Cor,Nor}})$ is equivalent to the interception of the ordinate



where the index s stands for the dehydrated moulding sand and the tube walls.

For an exact value of Σ_S a precise chemical analysis of the moulding sand is required. For a constant sand thickness Δz_S , this can be avoided by measuring the neutron transmission of the dry sand τ_S . Accordingly, $\Delta z_S \Sigma_S$ can be replaced by $-\ln(\tau_S)$:

$$\ln(\tau^{\text{Cor}}(x, y, t)) = \ln(\tau_S^{\text{Cor}}) - \Delta z_W(x, y, t) \Sigma_W \tag{9}$$

In this work, the specimen thickness in beam direction is not constant but well defined (Fig. 1). The sand and water transmission of the pyramidal part of the sample tube, therefore, can be normalized to the prismatic part of the sample tube by inserting a normalization factor $g(y)$:

$$g(y) = \begin{cases} 1.227 & \text{for } y \leq 0.5 \\ 1.341 - 0.227y & \text{for } 0.5 < y < 1.5 \\ 1 & \text{for } y \geq 1.5 \end{cases} \tag{10}$$

The relation for the corrected and normalized transmission then is:

$$\ln(\tau^{\text{Cor,Nor}}(x, y, t)) = \frac{\ln(\tau^{\text{Cor}}(x, y, t))}{g(y)} = \ln(\tau_S^{\text{Cor,Nor}}) - \frac{\Delta z_W(x, y, t) \Sigma_W}{g(y)} \tag{11}$$

With increasing water thickness, the relevance of multiscattering effects on the measured intensities increases. For a constant thickness of the porous medium, multiscattering can be taken into account by reference calibration measurements (Kang et al. 2013). Exchanging the product of the water thickness ($\Delta z_W(x, y, t)$) and the macroscopic cross section of water (Σ_W) by the water content ($w(x, y, t)$) and a correlation factor (Θ_W), the corrected and normalized transmission data ($-\ln(\tau^{\text{Cor,Nor}}(x, y))$) of the reference measurements can be plotted versus the moisture content of the reference sample (Fig. 2).

$$\ln(\tau_{\text{Ref}}^{\text{Cor,Nor}}(x, y)) = \ln(\tau_S^{\text{Cor,Nor}}) - \Theta_W w(x, y, t) \tag{12}$$

The slope and the intercept of the ordinate of the linear regression of reference transmission data yield the correlation factor (Θ_W) and the transmission of the dry sand ($\ln(\tau_S^{\text{Cor,Nor}})$), respectively. Therefore, the total moisture amount can be calculated by:

$$w(x, y, t) = \left(\ln \left(\tau_S^{\text{Cor,Nor}} \right) - \ln \left(\tau^{\text{Cor,Nor}}(x, y, t) \right) \right) / \Theta_W \tag{13}$$

For the calculation of the error of both the initial water content and the measured transmission, the equations from York et al. (2004) were applied using the MATLAB script from Thirumalai et al. (2011). In accordance with the law of error propagation, the maximum error in calculating the absolute water content can be assumed to be ± 0.65 wt.%:

$$\delta_w = \sqrt{\delta\Theta_W^2 + \delta \left(\ln \left(\tau_S^{\text{Cor,Nor}} \right) \Theta_W^{-1} \right)^2} = 0.65 \text{ wt.}\% \tag{14}$$

The high thermal conductivity of aluminium causes condensation of water at the tube walls. This condensation leads to water gradients in beam direction *z*. However, the water distribution in beam direction cannot be imaged in radiographs. Only the total transmission in *z*-direction can be measured. In order to assess the water inhomogeneity in beam direction, profiles were measured along the *y*-axes. In these *y*-profiles, the deviations between the average intensity and the intensity measured in the centre of the profile were never bigger than 1%. Assuming the *y*-profiles being representative for the beam direction *z*, water condensation at the tube walls contributes to the total error of the calculation of the water amounts by approximately less than 1%.

4 Results

From individual neutron radiographs taken at a given time (Fig. 3), the water contents were calculated along the central vertical profile by equation 13. The corresponding temperatures (Fig. 4) were allocated (Fig. 3a). All data were plotted versus time (Fig. 5). In experiments with identical parameters (initial sand moisture, sand compaction, heater temperature, heater

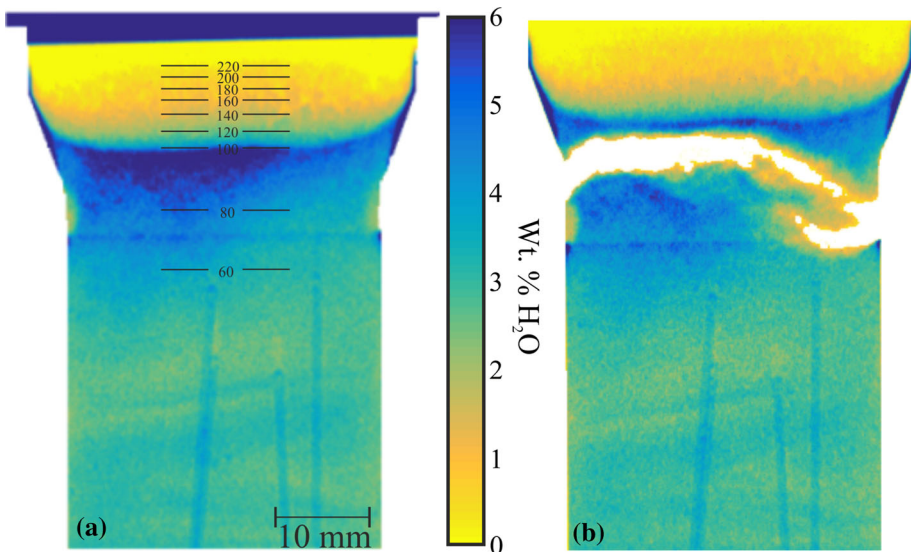


Fig. 3 Moisture distribution (colour coded) calculated by Eq. 13 from the radiographs taken 0.5 s before (a) and 0.5 s after (b) rupture. The temperature profile before rupture is given by isotherms (black lines in radiography a)

Fig. 4 Temperature evolution with time in three different experiments with an initial water content of 3 wt.% measured with thermocouples at three positions below the heating plate (0, 15, 30 mm)

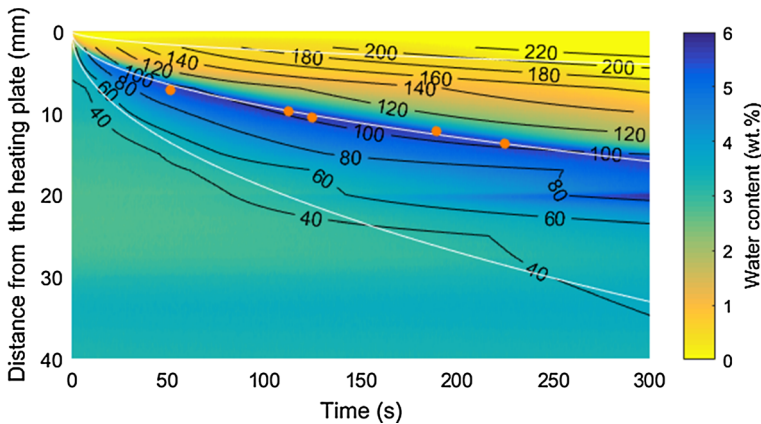
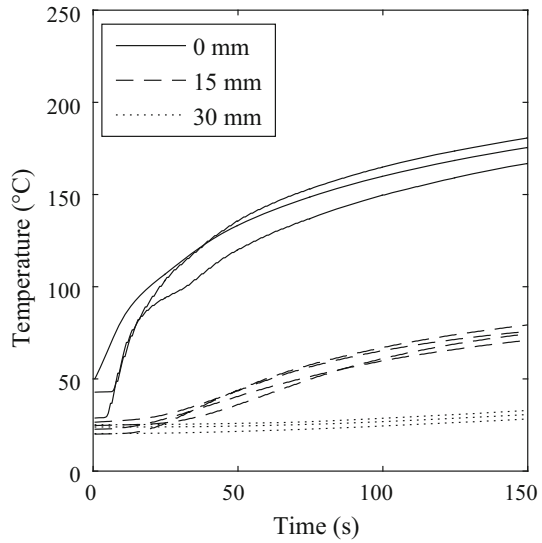


Fig. 5 Evolution of the moisture (colour coded) and temperature (black isotherms) during heating. The rupture positions from tensile tests after different heating times are marked by orange dots. Note, the different rupture positions were determined in a series of experiments with identical parameters and, therefore, identical heat and water kinematics. The white lines mark the boundaries between (from top to bottom) the dry zone, evaporation zone, condensation zone, and the external zone, respectively

power), water kinematics is highly reproducible. Within the spatial accuracy of water detection by neutron radiography, therefore, the moisture vs. time plots of different experiments with identical parameters are coincident.

Water evaporation starts instantaneously upon contact of sand specimen and heating plate. Steam diffuses into the sand interior where it condenses. An increase in the local water content in the condensation zone is the consequence (Fig. 6). After approximately 120 s, condensing steam reaches the interstice of the specimen tube (joining of lower base part and upper pyramidal part of the tube; Fig. 1). At the interstice, condensation is increased and, eventually, water is lost from the specimen by steam venting through the slit. Ignoring the

Fig. 6 Moisture distribution 30 (green), 60 (blue), 90 (turquoise), and 120 s (orange) after start of heating plotted versus the distance from the heating plate for sands with different initial moistures (solid line: 3 wt.% water, dashed line: 5 wt.% water)

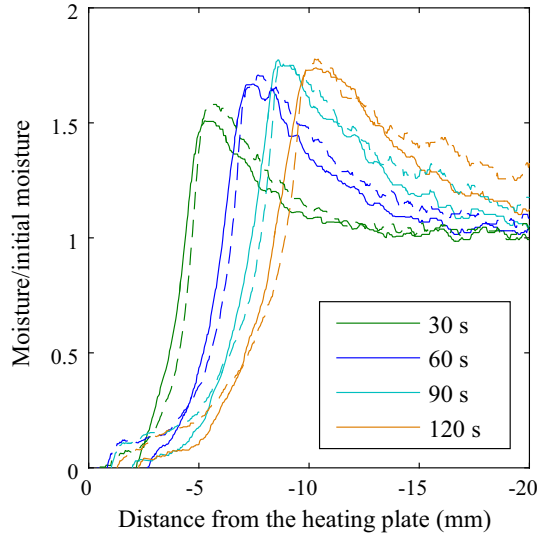
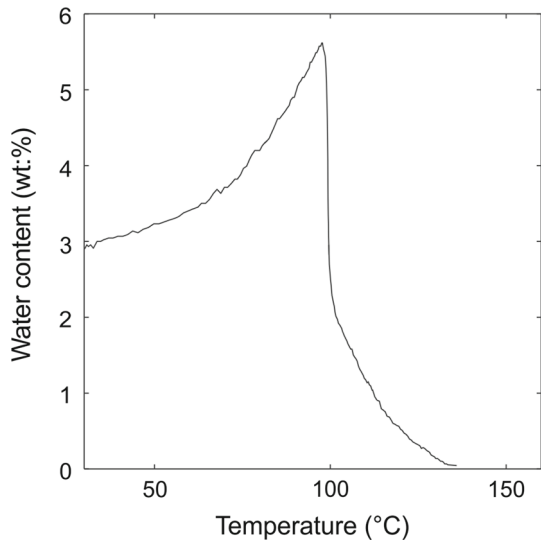


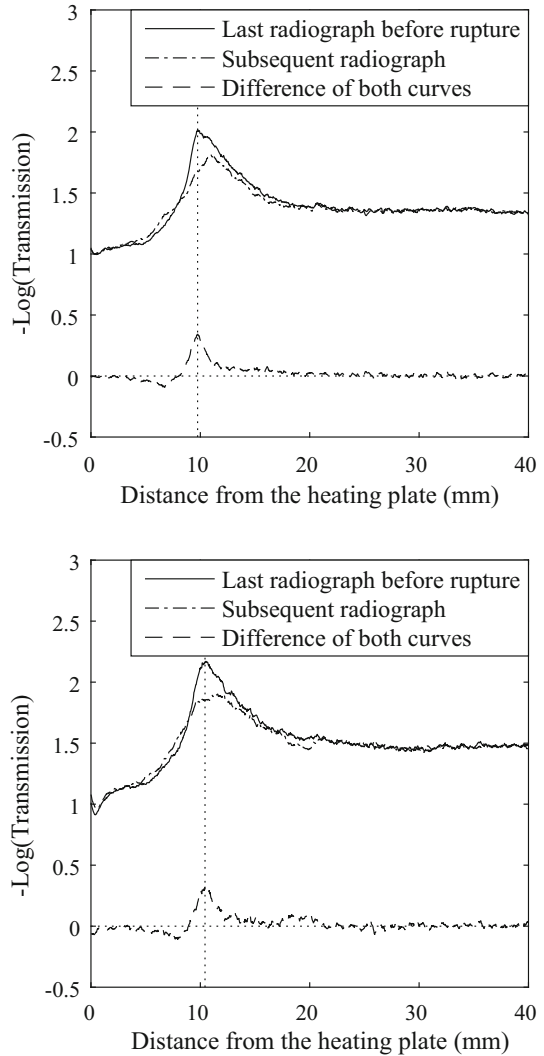
Fig. 7 Evolution of the water content measured at a thermocouple 5 mm beneath the heating plate versus the local temperature



interstice effect, the position of maximum local moisture correlates well with the 100 °C isotherm.

In the radiographs, water content can be measured at any given time and point of the sample—for instance at the position of a thermocouple. This water content can be plotted versus the momentary temperature reading of the thermocouple (Fig. 7). The experiments show that the water content first increases with increasing temperature and at $T \geq 100$ °C rapidly decreases. Dehydration continues to temperatures of approximately 140 °C. Between 140 and 310 °C no further increase of the neutron transmission (i.e. release of water or hydroxyls) can be observed.

Fig. 8 Negative natural logarithm of the horizontal transmission profiles of moulding sands (3 wt.% initial moisture) before rupture (solid line), 0.25 s later (dash-dot line), and their difference (dash line). Upper image and lower image taken after a heating period of 125 and 189 s, respectively. The maximum change indicates the rupture position exactly



If tensile stress is applied to the sample, neutron radiography allows an exact determination of the rupture location. Vertical profiles of the neutron transmissions were taken from the last radiograph recorded before rupture and from the directly subsequent radiograph (image acquisition frequency: 4 Hz). The negative natural logarithms of the transmissions were plotted together with the difference of the two profiles. The rupture position was allocated to the maximum difference (Fig. 8). The rupture positions were then inserted into the plots with the local water contents and temperatures (Fig. 5).

The rupture positions (within the tube interior) obtained by tensile testing at 51, 112, 125, 189, 225, and 315 s after contact with the heating plate (but otherwise identical parameters) were inserted in Fig. 5. The positions of the rupture plane within the tube interior closely follow the positions of the highest moisture content.

Fig. 9 Green (empty triangles) and wet (filled triangles) tensile strength versus moisture at the location of fracture. Triangles pointing in the same direction link experiments performed with identical moulding sand parameters, i.e. link green tensile strength of a given moulding sand with the respective wet tensile strength of this sand

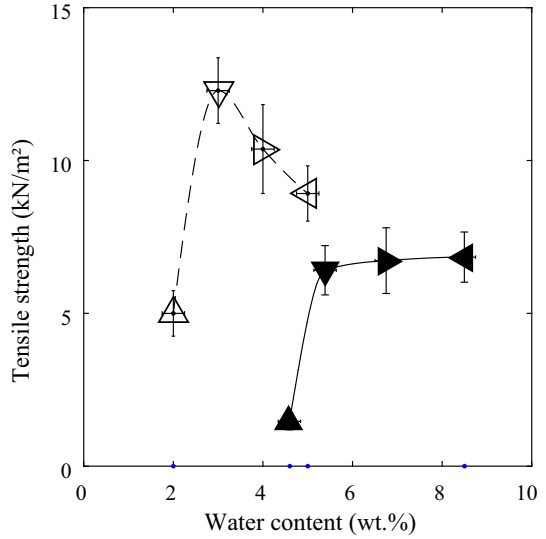
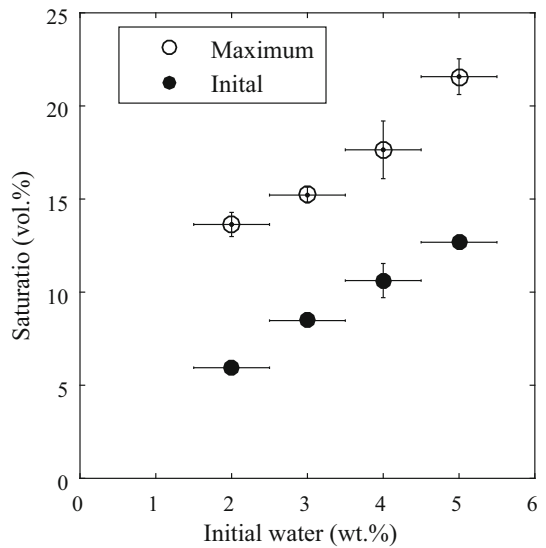


Fig. 10 Initial (filled dots) and maximum saturation (empty dots) plotted versus initial moisture. Saturation was calculated according to Eq. 2



From the measured tensile forces, wet tensile strengths (i.e. heated samples) and green tensile strengths (i.e. unheated samples) were calculated by Eq. 3. Both wet and green tensile strength depend on the initial moisture of the sand (Fig. 9). Green tensile strength initially increases for sands with increasing moisture and then shows a maximum of 12 kN/m at approximately 3 wt.% water, which corresponds to a saturation S of 0.09 (Fig. 10). Finally, the green tensile strength decreases to 7.8 kN/m at 5 wt.% initial water content with a saturation of 0.13. At all moisture contents, green tensile strength is higher than the related wet tensile strength. The wet tensile strength increases from 18 to 5.8 kN/m for sands with 2 and 3 wt.% initial water, respectively. A further increase of the initial moisture to 5 wt.% only causes a weak increase of wet tensile strength to 6 kN/m².

5 Discussion

5.1 Heat and Mass transfer

Models for heat-driven mass transport in porous media such as bentonite-bonded sand moulds were described, e.g. by Kubo and Pehlke (1986); Schröder and Macherauch (1977); Udell (1983); Starobin et al. (2011). Among these models, the model of Kubo and Pehlke (1986) is the most detailed one for coupled heat and mass transfer occurring during casting. Heat conduction, heat convection, condensation and evaporation were taken into account. At a given distance from the melt, equality of temperatures of water, quartz, and bentonite was assumed. Furthermore, heat transport by vapour transfer and by heat conduction between sand particles and vapour was taken into account. With respect to temperature, Kubo and Pehlke (1986) and Udell (1983) distinguished four zones with different transport characteristics. These four zones can be described in the unsteady-state system of this work in the following way:

1. The dry zone where the water has been vaporized completely. Here the moisture content is zero and the temperature is above 100 °C.
2. The evaporation zone where the temperature is 100 °C and moisture is decreasing at a certain position over time.
3. The condensation zone where the temperatures are between 100 °C and room temperature, and the moisture content is increasing at a certain position over time.
4. The external zone where temperature and moisture are unaffected by the casting process.

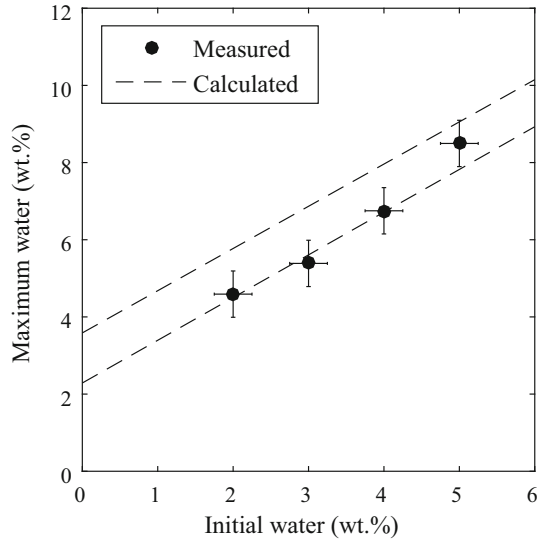
In the dry zone, heat is mainly transported by conduction in the solid phases. In the evaporation and condensation zone, heat transport additionally takes place by water vapour flow within the open pore space. This moisture transport is driven by pressure difference, diffusion, vaporization, and condensation.

Kubo and Pehlke (1986) defined the zone boundaries by isotherms assuming that the complete pore water evaporates at 100 °C. Exchange between pore water and water within the interlayers of the clay minerals was not taken into account. However, Fig. 7 shows that water does not completely evaporate from the moulding sand at 100 °C. This finding is in agreement with literature data which show that due to diffusion-controlled dehydration of water within the interlayers of smectites, some water can remain within the interlayers well above 100 °C (Odom 1984; Ferrage et al. 2010; Bray and Redfern 1999; Zabat and Van Damme 2000). As water remains in the moulding sand at temperatures up to 140 °C, the boundary between dry zone and evaporation zone has to be moved from the 100 °C isotherm to much higher temperatures.

The boundary between evaporation zone and condensation zone is marked by the location where the temperature of the sand is just reaching the boiling point of bulk water (i.e. pore water). The boundary, therefore, simultaneously represents the location of maximum water content (max). This maximum value of moisture is predominantly controlled by the heat capacity of the moulding sand environment (Kubo and Pehlke 1986; Patterson and Boenisch 1961). Once the heat of condensation raises the temperature up to the boiling point, maximum moisture is reached and the boundary between the evaporation and the condensation zone passes this location. According to Carslaw and Jaeger (1959), maximum moisture w_{\max} can be approximated by:

$$w_{\max} = w_0 + (w_0 C_w + (1 - w_0) C_s) \frac{373 - T_0}{L_W} \quad (15)$$

Fig. 11 Measured and calculated maximum water contents versus initial moisture. The calculations were performed with Eq. 15 using a specific heat C_s of moulding sand of 0.84 and 1.26 kJ/(kg K) as a lower and upper limit, respectively



where w_0 is the initial water, C_W the specific heat of water (approx. 4.2 kJ/(kg K)), C_s the specific heat of moulding sand, T_0 the initial temperature, and L_W the latent heat of evaporation (kJ/kg). The specific heat of moulding sand is between 0.84 and 1.26 kJ/(kg K) (Schröder and Macherauch 1977). The water contents calculated by Eq. 15 fit well with the measured values (Fig. 11).

Heat transfer in completely dry sand is maintained without vapour transfer, i.e. mainly by conduction. Therefore, the vertical extension (Δy_{Dry}) of the dry sand zone can be approximated by (Kubo and Pehlke 1986):

$$\Delta y_{Dry} = q\sqrt{t} \tag{16}$$

where q is the propagation constant. In foundry industries, Eq. 16 is also commonly used to describe the movement of the boundary between evaporation and condensation zone, i.e. the location of maximum moisture (Campbell 2011). In order to verify the applicability of Eq. 16 for the various zone boundaries, in situ neutron radiography can provide the required accurate experimental data. From moisture profiles along the centre of the specimen tube, the positions of the boundaries were determined in the radiographs. The boundary between the evaporation and condensation zone was allocated by the moisture maximum during the initial 120 s of the experiments. (After this period, water begins to vent through the tube interstice and positioning of the boundary becomes less accurate). Allocation of the boundaries between dry and evaporation zone as well as condensation and external zone is more problematic because the moisture gradients are asymptotic at these boundaries. The boundary between condensation and external zone, therefore, was defined by the position where the local moisture exceeds the initial water by more than 1%. The extent of the dry zone was defined by the range in which the local moisture content is less than 1% larger than at the end of the experimental run. The obtained positions of the zone boundaries can then be plotted versus the square root of time (Fig. 12). The data show that the propagation of all zone boundaries can be approximated by Eq. 16.

From the data in Fig. 12, the propagation constants q of the boundaries were calculated by least square fits. Boundary propagation constants were calculated from experiments with

Fig. 12 Evolution of the zone boundaries with the square root of time in experiments with an initial moisture of 3 wt.%

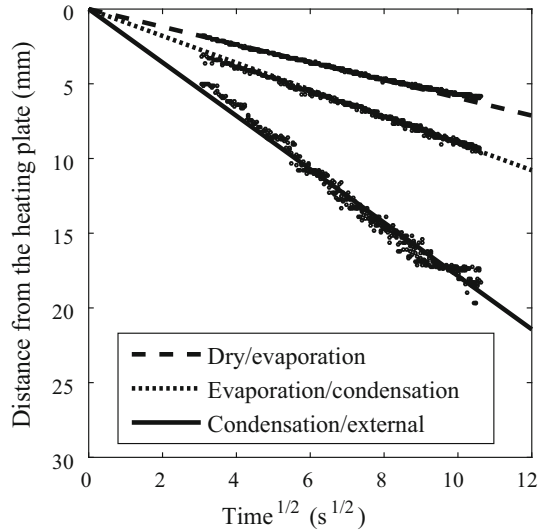
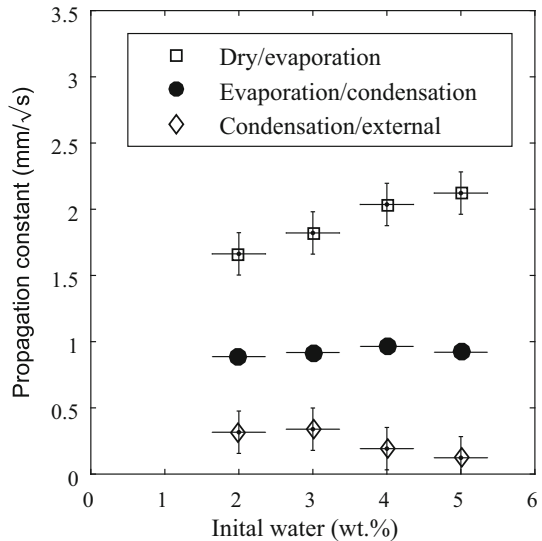


Fig. 13 Propagation constants of zone boundaries in moulding sands with different initial moisture contents



different initial moisture contents (2, 3, 4, and 5 wt.%; Fig. 13). The propagation constants of the boundary between dry and evaporation zone, which is primarily driven by heat conduction (Udell 1983; Kubo and Pehlke 1986), are nearly independent of the initial water content.

The propagation constants of the boundary between evaporation and condensation zone (Fig. 13) are in good agreement with Udell (1983). This author showed that the movement of the boundary is dominated by the vapour pressure gradient between dry and condensation zone, which is largely independent from initial moisture contents of the sand.

The propagation of the boundary between condensation and external zone (Fig. 13) is driven by water and steam diffusion (Udell 1983). The temperature at the hot end of the condensation zone is always 100 °C. Consequently, the gas pressure difference between both ends of the condensation zone is constant. With increasing initial moisture both the porosity

Fig. 14 Porosity calculated by Eq. 1 versus initial moisture

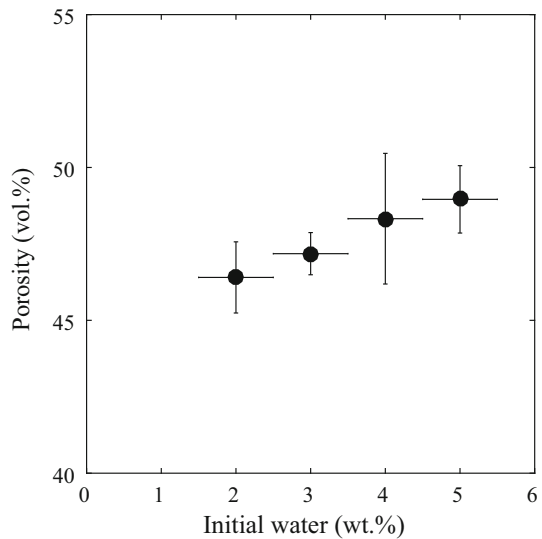


(Fig. 14) and the saturation of the pore space (Fig. 10) increase. Although the saturation of the pore space (Fig. 10) increases with increasing initial moisture, a significant effect of initial water content on gas permeability is not likely in the range of initial water contents of this experiment. However, the heat capacity of the mould increases with increasing initial moisture and causes an increase of the heat flux (Fan and Wen 2002). Consequently, the propagation constant of the boundary between condensation and external zone increases (Popielarski and Ignaszak 2016).

5.2 Tensile Strength

The dependence of green tensile strength (i.e. the tensile strength of the unheated sand) on sand moisture agrees well with the data of Patterson and Patterson and Boenisch (1961), who also observed a positive correlation of tensile strength with water content followed by a negative correlation at water contents larger than approx. 3 wt.%. The observed initial increase of green tensile strength with water content is in accordance with the numerical model derived by Lu et al. (2009) for the tensile strength of moist sands. For clay, the numerical model of Lu et al. (2010) yields a negative correlation of tensile strength with increasing moisture. The observed decrease of the green tensile strength at water contents higher than 3 wt.% (which corresponds to a saturation of less than 10 vol.%), therefore, may indicate that the mechanical behaviour of the moulding sand is increasingly dominated by the clay minerals. In this context, it has to be noted that the clay minerals in moulding sands are rolled onto the quartz grains by a milling process rather than loosely mixed with quartz grains. The porosity and texture of moulding sands, therefore, are strongly influenced by the quartz grains, while the clay minerals may affect the surface properties strongly.

The tensile strength of the unheated sand corresponds with the data of Patterson and Boenisch (1961) which also observed a strong increase of tensile strength with an increasing water content from 2 to 3 wt.% and a strong decrease when the water content increases further. The increase in tensile strength is in accordance with the theoretical model of Lu

et al. (2009) for sands. The decrease at higher water contents indeed indicates a clay-like behaviour (Lu et al. 2010).

The quantitative transport data as obtained from neutron radiographs coupled with the quantitative mechanical data obtained from tensile strength testing allow for an investigation of the effect of heat and mass transfer on the tensile strength as one of the most important properties of bentonite-bonded moulding sands. The data show that the tensile strength of moulding sands, which contain heat-driven evaporation and condensation zones, is significantly lower than the tensile strength of the same sands at room temperature (Fig. 9). Furthermore, the data show that this decrease in strength is taking place not homogeneously over the entire specimen. Consequently, a point of lowest tensile strength can be located which moves away from the heat source. The position of this weakest point depends on temperature and moisture content, both the present and in the past. In neutron radiographs, the weakest position can clearly be identified by the rupture plane. This plane coincides with the location of maximum water content and the position where the sand temperature reaches the boiling point of bulk water. The rupture plane, therefore, corresponds to the boundary of condensation and evaporation zone.

These findings partially contradict Patterson and Boenisch (1961) who assumed that the supersaturation in the condensation zone (i.e. in the zone of temperatures below the boiling point of water) is the main reason for spalling. Even though water contents exceeding approx. 3 wt.% cause decreasing tensile strengths within the condensation zone, the rupture positions observed in the present experiments clearly correlate with the distinct temperature and moisture conditions marked by the boundary of condensation and evaporation zone. As the position of this boundary depends on heat and moisture transfer, the location of minimum tensile strength is transient and moves into the mould interior continuously with time.

Tensile strength is related to a number of different forces and bonds (Wiebe et al. 1998; Lu et al. 2007; Tang et al. 2015) some of which depend more strongly on temperature and water content than others. In general, four different forces and bonds can be distinguished: (1) van der Waals force, (2) electrical double-layer forces between clay mineral surfaces, (3) capillary forces at water bridges, and (4) bonds between grains caused by mineral precipitates from evaporating water.

Following the reasoning of Munkholm and Kay (2002); Heibrock et al. (2005); Forsmo et al. (2006); Zeh and Witt (2007); Vanicek (2013), capillary force is the major force binding sand grains in moist sand. With increasing water content, the saturation increases. At first, more water bridges are formed and the number of capillary contacts between water and solid surfaces increases. With a further increase of the water content, however, the pore space becomes more saturated and the water bridges merge (Lu et al. 2007; Tang et al. 2015; Song et al. 2012). The surfaces of more and more grains become completely wetted, and the cohesion between the particles decreases. Above a critical water content, therefore, tensile strength decreases again.

Water content is not the only factor affecting tensile strength. The experiments show (Fig. 9) that the tensile strength of moulding sands with a water content for instance of 5% varies significantly with temperature. This is in accordance with Patterson and Boenisch (1961) who reported that moist sand has the highest tensile strength at room temperature. The decrease of tensile strength can be explained by the temperature dependence of capillary forces. Higher temperatures lead to a decrease of the surface tension of water (Young and Harkins 1928) and lower capillary forces. At the boiling point, surface tension of water and capillary forces become zero. The majority of water bridges therefore do not collapse within the condensation zone but at the boiling point.

Within the evaporation zone (i.e. the zone of temperatures at and above the boiling point of water), the residual tensile strength is related to both the binding capacity of bentonite, which is largely facilitated by the remaining water molecules still adsorbed at the clay surfaces, and the cementation caused by precipitation of solutes between the sand grains from evaporating water. While the binding capability of the first decreases with increasing temperature due to increasing water desorption from the surfaces, the binding capability of the latter increases with increasing temperature. Above 140 °C, finally, cementation within the virtually dry sand leads to a tensile strength which is much higher than that of moist sand (Patterson and Boenisch 1961). By image analyses and consideration of earlier works, the minimum tensile strength can be precisely located at the front of the evaporation zone.

6 Conclusion

Neutron radiography imaging was successfully applied to follow wet tensile testing in situ during heat application. Radiography enabled for both quantification of the water kinematics and determination of the location of lowest strength in the moisture profile. The preferred fracture position was pinpointed at the boundary between evaporation and condensation zone. We suggest that this location of minimum tensile strength could be explained by the negative correlation of the surface tension of water and temperature (Kayser 1976), which reaches minimum value at 100 °C, and by the onset of the boiling of the water within the water bridges, lowering the capillary force even more, and leading to the observed minimum of tensile strength. The results refute common postulations (Odom 1984; Campbell 2011; Patterson and Boenisch 1961) that the fracture occurs within the condensation zone, exclusively caused by the supersaturation of the sand.

Acknowledgements We sincerely thank the reviewers for constructive criticisms and valuable comments, which were of great help in revising the manuscript. The work is based upon experiments performed at ANTARES operated by FRM II at Heinz Maier-Leibnitz Zentrum (MLZ, Garching Germany) as well as at ICON at Paul Scherrer Institute (Villigen, Switzerland). Funding from DFG (JO301/5-1) is gratefully acknowledged. Excellent samples were kindly provided by S&B Industrial Minerals GmbH.

Open Access This article is distributed under the terms of the Creative Commons Attribution 4.0 International License (<http://creativecommons.org/licenses/by/4.0/>), which permits unrestricted use, distribution, and reproduction in any medium, provided you give appropriate credit to the original author(s) and the source, provide a link to the Creative Commons license, and indicate if changes were made.

References

- BDG: VDG - Merkblatt p38: Prüfung von tongebundenen Formstoffen Bestimmung der Festigkeit. Technical Report, Bundesverband der Deutschen Gießerei-Industrie BDG (1997)
- Boon, J.J., Hendrickx, R., Eijkel, G., Cerjak, I., Kaestner, A., Ferreira, E.S.B.: Neutron radiography for the study of water uptake in painting canvases and preparation layers. *Appl. Phys. A* **121**(3), 837–847 (2015)
- Bray, H., Redfern, S.: Kinetics of dehydration of Ca-montmorillonite. *Phys. Chem. Miner.* **26**(7), 591–600 (1999)
- Campbell, J.: *Complete Casting Handbook*, 1st edn. Elsevier, Amsterdam (2011)
- Carslaw, H.S., Jaeger, J.C.: *Conduction of Heat in Solids*, 2nd edn. Clarendon Press, Oxford (1959)
- Fan, J., Wen, X.: Modeling heat and moisture transfer through fibrous insulation with phase change and mobile condensates. *Int. J. Heat Mass Transf.* **45**(19), 4045–4055 (2002)
- Ferrage, E., Lanson, B., Michot, L.J., Robert, J.L.: Hydration properties and interlayer organization of water and ions in synthetic Na-smectite with tetrahedral layer charge. Part 1. Results from X-ray diffraction profile modeling. *J. Phys. Chem. C* **114**(10), 4515–4526 (2010)

- Forsmo, S., Apelqvist, A., Björkman, B., Samskog, P.O.: Binding mechanisms in wet iron ore green pellets with a bentonite binder. *Powder Technol.* **169**(3), 147–158 (2006)
- Grim, R.E., Guven, N.: *Bentonites—Geology, Mineralogy, Properties and Uses*. Elsevier, Amsterdam (1978)
- Hall, S.A.: Characterization of fluid flow in a shear band in porous rock using neutron radiography. *Geophys. Res. Lett.* **40**(11), 2613–2618 (2013)
- Harvey, C.C., Murray, H.H.: Industrial clays in the 21st century: a perspective of exploration, technology and utilization. *Appl. Clay Sci.* **11**(5), 285–310 (1997)
- Hassanein, R.: Correction methods for the quantitative evaluation of thermal neutron tomography. Ph.D. thesis, Swiss Federal Institute of Technology Zürich (2006)
- Hassanein, R., Meyer, H.O., Carminati, A., Estermann, M., Lehmann, E., Vontobel, P.: Investigation of water imbibition in porous stone by thermal neutron radiography. *J. Phys. D Appl. Phys.* **39**, 4284–4291 (2006)
- Heibrock, G., Zeh, R.M., Witt, K.J.: Tensile strength of compacted clays. In: Schanz, T. (ed.) *Unsaturated Soils: Experimental Studies*, pp 395–412. Springer, Berlin (2005)
- Jordan, G., Eulenkamp, C., Calzada, E., Schillinger, B., Hoelzel, M., Gigler, A., Stanjek, H., Schmahl, W.W.: Quantitative in-situ study of the dehydration of bentonite-bounded moulding sands. *Clays Clay Miner.* **61**(2), 133–144 (2013)
- Kaestner, A., Lehmann, E., Stampanoni, M.: Imaging and image processing in porous media research. *Adv. Water Resour.* **31**, 1174–1187 (2008)
- Kaestner, A., Hartmann, S., Kühne, G., Freib, G., Grünzweig, C., Josic, L., Schmid, F., Lehmann, E.: The ICON beamline—a facility for cold neutron imaging at SINQ. *Nucl. Instrum. Methods Phys. Res. Sect. A* **659**(11), 387–393 (2011)
- Kang, M., Bilheux, H., Voisin, S., Cheng, C., Perfect, E., Horita, J., Warren, J.: Water calibration measurements for neutron radiography: application to water content quantification in porous media. *Nucl. Instrum. Methods Phys. Res. Sect. A* **708**, 24–31 (2013)
- Kayser, W.V.: Temperature dependence of the surface tension of water in contact with its saturated vapor. *J. Colloid Interface Sci.* **56**(3), 622–627 (1976)
- Kubo, K., Pehlke, R.D.: Heat and moisture transfer in sand molds containing water. *Metall. Trans. B* **17**(4), 903–911 (1986)
- Lu, N., Wu, B., Tan, C.P.: Tensile strength characteristics of unsaturated sands. *J. Geotech. Geoenviron. Eng.* **133**(2), 144–154 (2007)
- Lu, N., Kim, T.H., Sture, S., Likos, W.J.: Tensile strength of unsaturated sand. *J. Eng. Mech.* **135**(12), 1410–1419 (2009)
- Lu, N., Godt, J.W., Wu, D.T.: A closed-form equation for effective stress in unsaturated soil. *Water Resour. Res.* **46**(5), W05515 (2010)
- Munkholm, L.J., Kay, B.D.: Effect of water regime on aggregate-tensile strength, rupture energy, and friability. *Soil Sci. Soc. Am. J.* **66**, 702–709 (2002)
- Odom, I.E.: Smectite clay minerals: properties and uses. *Philos. Trans. R. Soc. Lond. A Math. Phys. Eng. Sci.* **311**(1517), 391–409 (1984)
- Patterson, W., Boenisch, D.: Die Bedeutung der Festigkeit feuchter, tongebundener Formsande insbesondere der Naßfestigkeit. *Giesserei* **3**, 157–193 (1961)
- Patterson, W., Boenisch, D.: Das Schülpendiagramm für Naßzugsande. *Giesserei* **51**(21), 634–641 (1964)
- Popielarski, P., Ignaszak, Z.: Effective modelling of phenomena in over-moisture zone existing in porous sand mould subjected to thermal shock. In: Delgado, J.M.P.Q., Gilson Barbosa de Lima, A. (eds.) *Drying and Energy Technologies*, pp 181–206. Springer, Cham (2016)
- Schillinger, B., Calzada, E., Lorenz, K.: Modern neutron imaging: radiography, tomography dynamic and phase contrast imaging with neutrons. *Solid State Phenom.* **112**, 66–72 (2006)
- Schillinger, B., Calzada, E., Eulenkamp, C., Jordan, G., Schmahl, W.W.: Dehydration of moulding sand in simulated casting process examined with neutron radiography. *Nucl. Instrum. Methods Phys. Res. Sect. A* **651**(1), 312–314 (2011)
- Schröder, A., Macherauch, E.: Zur Temperaturverteilung in strahlungsbeheizten ebenen Formdecken aus tongebundenem Quarzsand. *Giessereiforschung* **29**(1), 41–46 (1977)
- Schulz, M., Schillinger, B.: Antares: cold neutron radiography and tomography facility. *J. Large Scale Res. Facil.* **1**(A17), 1–4 (2015)
- Sedighi-Gilani, M., Wakili, K.G., Koebel, M., Hugi, E., Carl, S., Lehmann, E.: Visualizing moisture release and migration in gypsum plaster board during and beyond dehydration by neutron radiography. *Int. J. Heat Mass Transf.* **60**, 248–290 (2013)
- Shokri, N., Or, D.: Drying patterns of porous media containing wettability contrasts. *J. Colloid Interface Sci.* **391**, 135–141 (2013)
- Shokri, N., Lehmann, P., Vontobel, P., Or, D.: Drying front and water content dynamics during evaporation from delineated by neutron radiography. *Water Resour. Res.* **44**, W06418 (2008)

- Song, Y.S., Hwang, W.K., Jung, S.J., Kim, T.H.: A comparative study of suction stress between sand and silt under unsaturated conditions. *Eng. Geol.* **124**(W06418), 90–97 (2012)
- Starobin, A., Hirt, T., Lang, H., Todte, M.: Core drying simulation and validation. *Am. Foundry Soc. Proc.* **11–028**, 1–5 (2011)
- Tang, C.S., Pei, X.J., Wang, D.Y., Shi, B., Li, J.: Tensile strength of compacted clayey soil. *J. Geotech. Geoenviron. Eng.* **141**(4), 04014,122 (2015)
- Thirumalai, K., Singh, A., Ramesh, R.: A matlab™ code to perform weighted linear regression with (correlated or uncorrelated) errors in bivariate data. *J. Geol. Soc. India* **77**(4), 377–380 (2011)
- Udell, K.S.: Heat transfer in porous media heated from above with evaporation, condensation, and capillary effects. *J. Heat Transf.* **105**(3), 485–492 (1983)
- Vanicek, I.: The importance of tensile strength in geotechnical engineering. *Acta Geotech. Slov.* **1**, 5–9 (2013)
- Villman, B., Slowik, V., Wittmann, F.H., Vontobel, P., Hovind, J.: Time-dependent moisture distribution in drying cement mortars—results of neutron radiography and inverse analysis of drying tests. *Restor. Build. Monum.* **20**(1), 49–62 (2014)
- Wiebe, B., Graham, J., Tang, G.X., Dixon, D.: Influence of pressure, saturation, and temperature on the behaviour of unsaturated sand-bentonite. *Can. Geotech. J.* **35**(2), 194–205 (1998)
- Wolters, F., Baille, W., Emmerich, K., Schmidt, E., Wolters, C., Königer, F., Kunz, J., Krase, V., Schellhorn, M.: High-density bimodal bentonite blends for hydraulic sealings at the ibbenbüren coalmine. *Clay Miner.* **50**(3), 391–403 (2015)
- York, D., Evensen, N.M., Martinez, M.L., De Basabe, Delgado J.: Unified equations for the slope, intercept, and standard errors of the best straight line. *Am. J. Phys.* **72**(3), 367–375 (2004)
- Young, F., Harkins, W.D.: *International Critical Tables of Numerical Data, Physics, Chemistry and Technology*, vol. 4. McGraw-Hill, New York (1928)
- Zabat, M., Van Damme, H.: Evaluation of the energy barrier for dehydration of homoionic (Li, Na, Cs, Mg, Ca, Ba, Alx(OH)_y^{z+} and La)-montmorillonite by a differentiation method. *Clay Miner.* **35**(2), 357–363 (2000)
- Zeh, R.M., Witt, K.J.: The tensile strength of compacted clays as affected by suction and soil structure. In: Schanz, T. (ed.) *Experimental Unsaturated Soil Mechanics*, pp 219–226. Springer, Berlin (2007)